Tidal current turbine in a non-homogeneous turbulent inflow: performance and near wake statistics

Ashwin Vinod and Arindam Banerjee

***Abstract*— In light of the 2018 special report on climate change compiled by the United Nations, there is a renewed urgency to the rapid adoption of renewable energy technologies. A key roadblock to the large-scale/commercial conversion of tidal energy is the question concerning the operational efficiency of existing technologies in the non-homogeneous, turbulent and corrosive marine environment. A thorough understanding of the aforementioned aspects of full-scale deployment is vital in developing robust and cost-effective turbine designs and farm layouts. The current experimental work at Lehigh University aims to better the understanding of turbine performance and near-wake statistics in homogeneous and non-homogeneous turbulent flows, similar to actual marine conditions. A 1:20 laboratory scale tidal turbine model with a rotor diameter of 0.28m is used in the experiments and an active grid type turbulence generator, designed in-house, is employed to generate both homogeneous and non-homogeneous turbulent inflow conditions. To the knowledge of the authors, this is the first experimental study to explore the effects of non-homogeneous inflow turbulence on tidal turbines. From the data collected it was observed that the non-homogeneous inflow condition led to a considerable drop (15-20%) in the measured thrust coefficient. They also resulted in larger torque and thrust fluctuations on the rotor (~40% under the tested conditions). The effect of inflow non-homogeneity was evident in the asymmetric near-wake characteristics as well. Turbulence intensity and Reynolds stresses measured in the wake of the rotor were found to adapt quicker to inflow non-homogeneity than the wake velocity deficit and integral length scales.**

***Keywords*— Active Grid, Homogeneous turbulence, Near-wake characteristics, Non-homogeneous turbulence, Performance characteristics, Tidal current turbine, Turbulence intensity.**

I. INTRODUCTION

ALL across the globe there is a growing demand for the rapid adoption of renewable energy resources[1].The tidal activity in the oceans is considered to be a highly predictable renewable energy resource[2]. In the last decade, tidal energy converters have undergone substantial improvements through numerous lab-scale experiments, computational investigations, analytical calculations, as well as a few field studies. At this time, it is relatively well documented the operation of tidal turbines varies with inflow direction [3], tip speed ratio [4], blade pitch [5, 6], inflow oscillations [7], support structure effects [8, 9], and bounding surface proximity[10-12]. In addition, turbine wake characteristics, in the near wake (until 5 diameters (D) downstream from the rotor) as well as far wake (beyond 5D) have been studied extensively[13-15] with an intent to design farms of tidal energy converters. However, studies demonstrating the effects of turbulent inflows (homogeneous and non-homogeneous inflows) on tidal turbines are comparatively limited[16, 17]. Tidal flows are considerably turbulent in nature. A majority of the full-scale demonstration designs tested are bottom mounted, and therefore are likely to be subjected to non-homogeneous inflow conditions owing to local bathymetry effects[18]. One-dimensional turbulence intensity, Ti, is defined as

$$Ti = 100\frac{\sigma(u)}{U} \quad (1)$$

where $\sigma(u)$ is the standard deviation of principal velocity samples, and U is the corresponding time-averaged value. Ti levels vary with respect to the site, time and location within a site. Several studies have assessed resource characteristics at tidal sites in the U.S. and U.K, and in most cases have observed a mean velocity between 1.3-2.5 m/s with elevated levels of Ti in the 8% - 13% range; the only exception to this being the East River in New York, where, Ti levels in the 20% - 30% range were recorded.

The effects of elevated, uniform Ti levels on turbine performance and wake characteristics have been explored in a few studies reported in the literature. Blackmore *et al.* [19] tested solid and porous disc turbine simulators in different levels of inflow Ti and observed a considerable effect on the measured drag coefficient. They noticed that the drag coefficient calculated at Ti >13% was 20% larger than the drag coefficient calculated at Ti<4.5%. Blackmore *et al.*[20] also explored the wake characteristics of an actuator disc in elevated Ti (5-10%) using large eddy simulation (LES). They predicted that the enhanced cross stream momentum diffusion in a turbulent environment would result in a quicker recovery of wake velocities.

Paper # 1455 was submitted to the "Tidal device development (TDD) and testing track" at EWTEC2019. Financial support for this work came from the U.S. National Science Foundation (Award # 1706358) through the CBET-Fluid Dynamics Program. A. Vinod (email: asv312@lehigh.edu) is a Ph.D. student working with Prof. Arindam Banerjee (*Corresponding author, email: arb612@lehigh.edu) as a part of the Turbulent Flow Design Group, in the Department of Mechanical Engineering & Mechanics at Lehigh University, Bethlehem, Pennsylvania, U.S.A.

Mycek *et al.* [17, 21] were the first to experimentally test the effect of inflow *Ti* on a lab-scale tidal turbine model. Their experiments were conducted in the IFERMR (French Research Institute for Exploitation of the Sea) wave and current flume tank, at two different levels of *Ti*; 3% (generated with flow conditioning) and 15% (generated without flow conditioning). They observed that the elevated inflow turbulence aggravated the fluctuations in measured thrust and torque values and led to a ~10% drop in averaged power. More recently, Blackmore et al.[16] experimentally tested a lab scale tidal turbine in *Ti* levels ranging from 5%-25% generated using passive grids. In addition to measuring the cumulative loads acting on the rotor, they measured blade root bending moments for the different cases and observed a 5-fold increase in blade load fluctuations in the most extreme *Ti* tested. They also proposed that the fatigue loads acting on the turbine can be estimated from the fluctuations observed in the power output and could be used to optimize maintenance operations without the need for additional monitoring instrumentation. Studies that have explored the effects of non-homogeneous turbulent inflows or sheared flows are even fewer. Rourke et al.[22] used an unsteady BEM model to perform a hydrodynamic analysis of a tidal current turbine in tidal current shear. They simulated multiple sheared inflow profiles and observed significant asymmetric loading on the rotor blade sections. Ahmed et al.[23], performed LES simulations of a full-scale tidal turbine in a non-homogeneous turbulent inflow representative of a tidal site, and captured the full spectrum of loads acting on the rotor. They also briefly discussed the wake characteristics of the turbine obtained through the simulations; however, did not compare it to experimental results due to the unavailability of such data sets.

The presented experimental work utilizes a Makita[24] type active grid turbulence generator to create, for the first time, a non-homogeneous turbulent inflow profile within a water tunnel facility, and study its effects on the performance and near wake characteristics of a lab-scale tidal turbine model. The data collected is discussed in detail by comparing it to the trends observed in a homogeneous turbulent inflow and a baseline laminar flow. The turbine performance characteristics are discussed in terms of the time-averaged power and thrust coefficients and their respective standard deviations. The near-wake region of the rotor is analyzed by examining the velocity deficit, turbulence intensities, Reynolds stresses, and integral length scales. Accurate prediction of turbine wakes is central to developing efficient tidal farm layouts. Though restricted to the near wake region, the current datasets can be used to validate and refine numerical models to better predict the complex flow patterns immediately downstream of a rotor[25]. The presented wake velocity profiles can also be used as inflow profiles for turbines to mimic wake interaction in a non-homogeneous turbulent environment without having to simulate multiple rotors.

II. Experimental Methods

The experimental work presented in this paper was performed in the water tunnel facility housed at Lehigh University. It has an open surface test section that is 0.61m wide, 0.61m tall and 1.98m long, and can reach flow velocities as high as 1 m/s.

A. Tidal turbine model

A three-bladed tidal turbine model with a rotor diameter (*D*) of 0.2794m was used in the current experiments[26] (see Fig.1). The constant chord (*c* = 0.0165m), no twist blades used in the rotor were made of corrosion resistant aluminum alloy with an SG6043 cross-section. With a rotor area of 0.0613 m^2, the turbine model operates at a blockage ratio (rotor area/cross-section of the test section) of 16% while operating in the Lehigh water tunnel facility. A stepper motor (Anaheim Automation, Model# 23MDSI) connected to the rotor via a stainless-steel shaft is used for the precise control of rotor rotational speeds. The loads acting on the rotor are measured using a sensor assembly within the nacelle; its primarily a combination of a thrust (Interface, Model# SML-25) and a torque sensor (Interface, Model# MRT2P) that decouples and evaluates the thrust and torque components of the loads acting on the turbine rotor. The manufacturer prescribed non-repeatability of the two sensors were ±0.0334N and ±0.001Nm respectively and were more sensitive than the load cell versions utilized in the previous experiments by the authors[10, 26]. The turbine nacelle was maintained pressurized (~20 kPa gauge pressure) to forestall the possibility of water damage to the electronic components in the assembly.

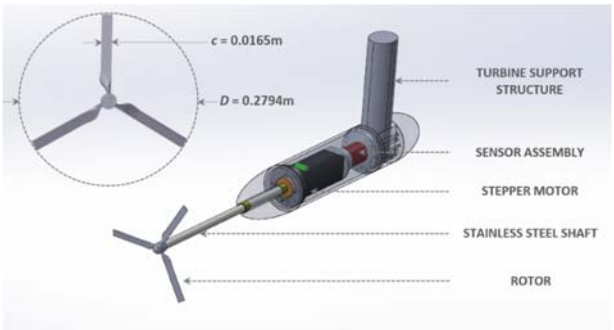

Fig. 1. Schematic of the 1:20 laboratory scale tidal turbine model used in the current study

B. Turbulence generator

A Makita type active grid turbulence generator[24] was used in the current experiments (see Fig. 2(a)). The inner cross-section of the active grid module was designed to precisely match the dimensions of the water tunnel test section. It housed a total of ten rotating winglet shafts; five oriented horizontally and five vertically. It was capable of operating in an alternate five shaft configuration with the

horizontal shafts alone. Six square winglets (0.06m x 0.06m) were attached to each of the shafts in a diamond fashion (diagonals aligned to the shaft axis), and adjacent shafts were separated by a distance of 0.1m, resulting in mesh size, *M* of 0.1m. The horizontal and vertical shafts were arranged in a bi-planar configuration and were controlled by a dedicated stepper motor, (Anaheim Automation, Model No. 23MDSI) which included an on-board simple controller/indexer and a micro-stepping driver. In addition to the rotating main winglets (a total of 60 in the ten-shaft configuration), the grid is also equipped with 24 non-rotating, corner winglets, along with the inner perimeter of the active grid frame, upstream of the plane of rotating winglets. Three forcing protocols, synchronous protocol (SP), single random protocol (SRP), and double random protocol (DRP) commonly used in literature were implemented using LabVIEW interface (see Fig. 2(b) for schematic). In SP, the winglet shafts rotate at constant and identical angular velocities with adjacent shafts rotating in opposite directions to eliminate the occurrence of mean vorticity in the resulting turbulent flow. SRP maintains a constant angular velocity across all shafts; however, randomly varies the direction of rotation from one shaft to the other. In DRP, both the parameters, angular velocity and direction of rotation are randomized for the different shafts. Compared to SP and SRP, DRP produces higher turbulence intensities and better isotropy and homogeneity[27].

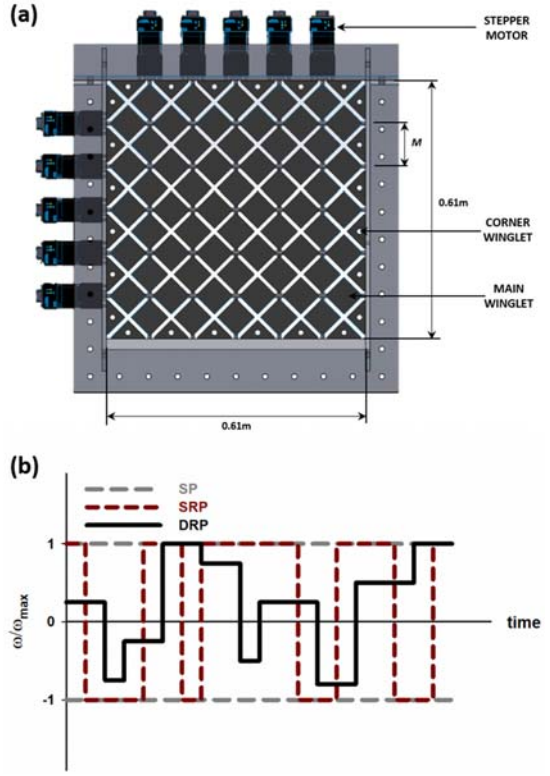

Fig. 2. (a) Schematic of the active grid turbulence generator, (b) Schematic of the programmed forcing protocols. (ω is the angular velocity of winglet shafts in radians/s)

C. Data analysis

1) Rotor load measurements

The thrust (*T*) and torque (*Q*) loads acting on the rotor were sampled at the rate of 200 samples/second. To identify an adequate sampling duration for load measurements, a 300s long time trace of loads was segmented into bins and analyzed. For each parameter of interest, a sampling period dependent *% Error* (defined in the equation) was estimated as

$$\%Error = 100\left|\frac{X_n - X_m}{X_m}\right| \tag{2}$$

where, X_n is the value of a parameter calculated from the complete time trace (300 seconds long in this case), and X_m is the value of the same parameter calculated from shorter, n seconds long time traces with n ranging from 1-300 seconds. The sampling period dependence of time-averaged *T* and *Q*, and their respective standard deviations $\sigma(T)$ and $\sigma(Q)$ are shown in Fig. 3(a). It can be noticed that *T*, *Q*, and $\sigma(Q)$ fall below a 3% error within 30 seconds of sampling, whereas, $\sigma(T)$ takes a longer period of ~ 60 seconds to drop below the 3% error mark. Therefore, to minimize errors in calculated performance parameters, the loads acting on the rotor were sampled for a period of 120 seconds. The non-dimensional parameters, the coefficient of power (C_P), the coefficient of thrust (C_T) and tip speed ratio (*TSR*) defined below, were used to characterize the turbine performance.

$$C_P = \frac{Q\Omega}{0.5\rho A U_\infty^3} \tag{3}$$

$$C_T = \frac{T}{0.5\rho A U_\infty^2} \tag{4}$$

$$TSR = \frac{R\Omega}{U_\infty} \tag{5}$$

Ω is the angular velocity of the rotor (rad/s), U_∞ is the area averaged freestream velocity (m/s), ρ is the density of water (kg/m^3), and *A* is the area of the rotor (m^2). The obtained non-dimensional coefficients were blockage corrected using the method described in Bahaj et al.[5].

2) Flow characterization

A Nortek Vectrino+ acoustic Doppler velocimeter (ADV) was used to perform all flow velocity measurements reported in this paper. The instrument had a measurement accuracy of ±0.005 m/s. The sampling frequency of 50Hz and a sampling volume of 1.7×10^{-7}m^3 was maintained across all measurements. Spike noticed in the obtained time traces were eliminated using the phase space thresholding (PST) technique described in Goring and Nikora[28]; the identified spikes were replaced using the mean value of the time trace.

Following Reynolds decomposition, each velocity component $u(t)$ (also $v(t)$and $w(t)$) can be broken down as follows

$$u(t) = U + u'(t) \tag{6}$$

into a time-averaged component, U and a time-dependent fluctuating component $u'(t)$. The non-dimensional Reynolds stress component R_{XZ}, and the integral length scale L, are computed as follows

$$R_{XZ} = \frac{\sqrt{\left|\frac{1}{N}\sum_{1}^{N} u_i' w_i'\right|}}{U} \tag{7}$$

$$L = U\int_0^T \frac{R(s)}{R(0)} ds \tag{8}$$

with, N being the total number of samples, T the corresponding total sampling period, s the time lag, and $R(s)$ the autocovariance defined as

$$R(s) = \langle u'(t)u'(t+s)\rangle \tag{9}$$

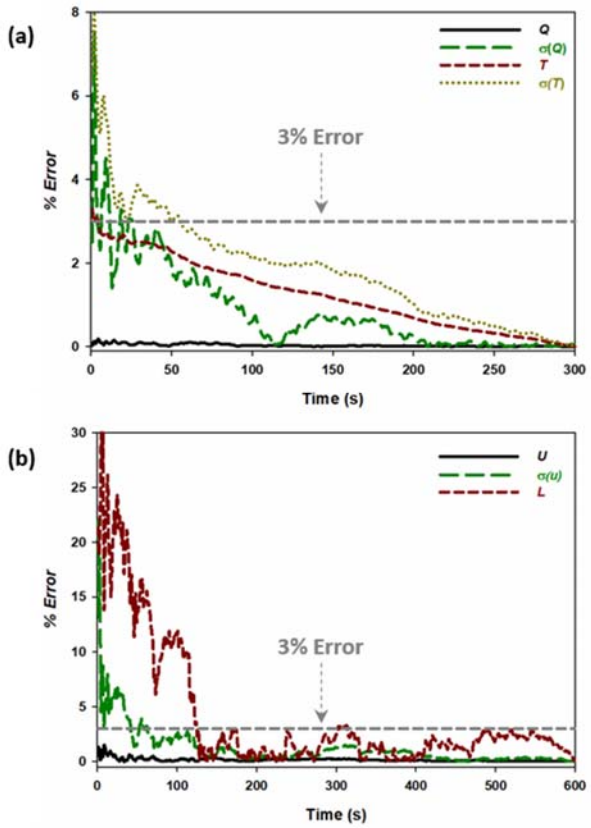

Fig. 3. (a) Effect of sampling period on load characteristics T, Q, $\sigma(T)$ and $\sigma(Q)$, (b) Effect of sampling period on flow characteristics U, $\sigma(u)$ and L

Similar to load measurements, a 600 seconds long time trace was collected and analyzed to assess convergence trends of the different flow parameters of interest. Fig. 3(b) shows the sampling period effects on U, $\sigma(u)$ and L. The %Error in U can be seen to converge almost immediately just within a few seconds; $\sigma(u)$ and L however, took longer to converge and fell below a 3% error mark beyond 60 seconds and 120 seconds respectively. Therefore, a sampling period of 120 seconds was maintained for all the flow measurements as well.

III. Results & Discussion

The different inflow conditions generated in the water tunnel facility using the active grid turbulence generator, and its effect on the performance and near-wake characteristics of the tidal turbine model is discussed in this section. All experiments reported in this paper were conducted at mean inflow velocities > 0.82 m/s, as Reynolds number effects on the turbine model used were found to minimal beyond 0.82 m/s[26]. To overcome the considerable blockage effects associated with the 10-shaft configuration of the active grid at such high inflow velocities, a 5-shaft configuration (horizontal shaft only) was adopted in this study (see Fig. 4. for a schematic of the experimental arrangement used).

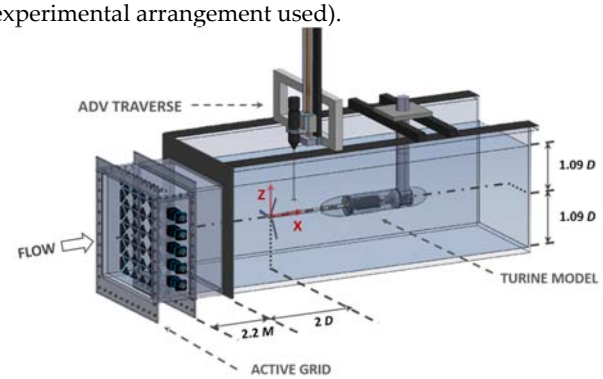

Fig. 4. Schematic of the experimental arrangement with the 5-shaft configuration of the Active Grid.

D. *Characterizing the inflow conditions*

The three distinct inflow conditions used in the experiments are listed below:

- Laminar flow (LF) - A near laminar (low turbulence) inflow obtained in the absence of active grid.
- Homogeneous turbulent inflow (HT) – Generated using the active grid operating in the double random forcing protocol with a maximum winglet shaft angular velocity (ω_{max}) of 3.14 radians/sec.
- Non-homogeneous turbulent inflow (NHT)– Generated using the active grid in a static mode. The horizontal winglet shafts were oriented in such a fashion that the blockage (obstruction to the flow) due to shaft winglets varied gradually from its highest value for the bottom-most shaft (winglets perpendicular to the flow) to its least value (winglets parallel to the flow) for the top-most shaft.

The inflows were assessed by making flow measurements across the depth (Z coordinate) of the tunnel at $X/D = 0$ in the absence of the turbine. The depth-wise variation of U and Ti for the three cases is plotted in Fig. 5.

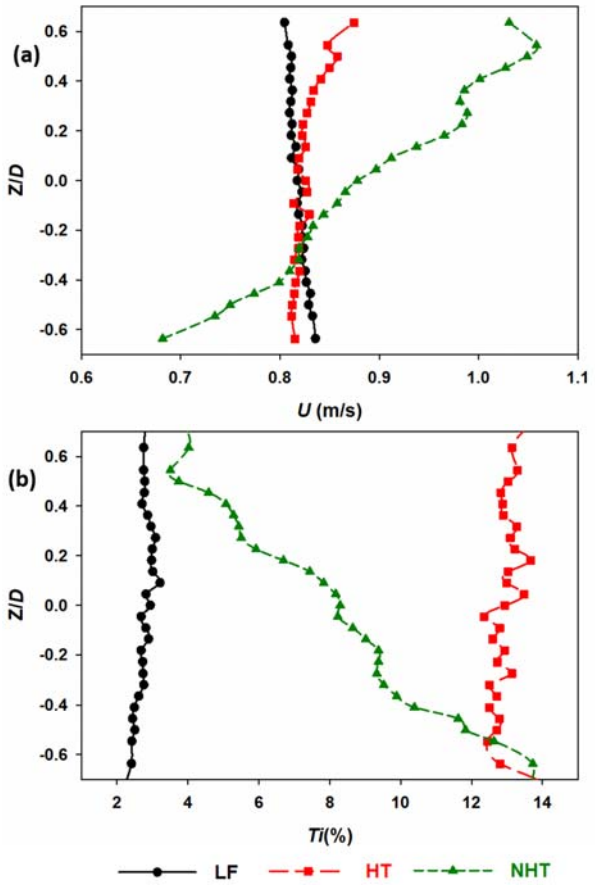

Fig. 5. Depth-wise variation of (a) inflow velocity (U), and, (b)streamwise turbulence intensity (Ti)

The laminar flow and the homogeneous turbulent inflow cases can be noticed to have a near uniform inflow velocity; U averaged across the rotor depth was estimated to be 0.82 m/s in the laminar flow and 0.83 m/s in the homogeneous turbulent inflow. The deviations in mean velocity for the above two cases were restricted to values < 2% of the depth-averaged mean for the most part, except at $Z/D > 0.45$ in the homogeneous turbulent flow, where it reached values as high as ~5%. Similar to U, the depth-wise variation in Ti for the laminar and homogeneous turbulent inflows were also found to be minimal; for the two cases, Ti across the depth of the rotor was found to be remain contained within 2.8±0.4% and 13±0.7% respectively. The non-homogeneous turbulent inflow, on the other hand, was composed to have a significant depth-wise variation of flow velocity ranging from ~ 0.7m/s at the bottom of the rotor to ~1m/s at the top end of the rotor. In addition, Ti across the depth of the rotor was tuned to vary from ~15% at the bottom of the rotor to ~4% at the top end of the rotor, mimicking the increased turbulence with depth observed in natural tidal flows. To better compare the non-homogeneous turbulent inflow to the laminar and homogeneous turbulent inflow cases, the depth-wise variability (or non-homogeneity) of the U and Ti across the rotor can be represented as 0.85±0.15m/s and 9.5±5.5% respectively. Table 1 lists the variation in mean velocity and turbulence intensity for all the three inflow cases.

TABLE I
VARIATION IN DEPTH-WISE VELOCITY AND TURBULENCE INTENSITY FOR THE DIFFERENT INFLOW CONDITIONS TESTED

Case	Inflow velocity range (m/s)	Turbulence Intensity Range (%)
Laminar Flow (LF)	0.82 ± 0.012	2.8 ± 0.4
Homogeneous Turbulent Flow (HT)	0.83 ± 0.03	13 ± 0.7
Non-Homogeneous Turbulent Flow (NHT)	0.85 ± 0.15	9.5 ± 5.5

E. Turbine performance characteristics

1) Power and thrust coefficient

The performance characteristics of the turbine were evaluated in the laminar, homogeneous and non-homogeneous turbulent inflow conditions.

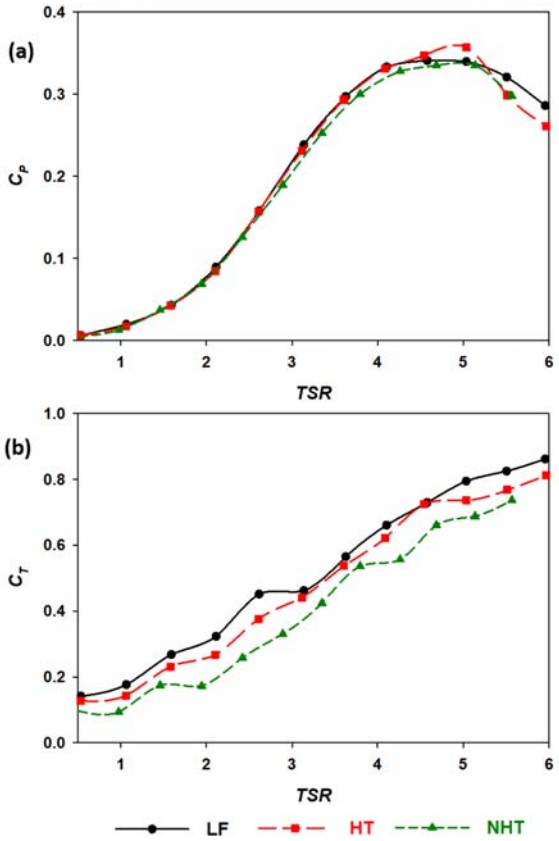

Fig. 6. Effect of inflow conditions on (a) C_P, (b) C_T

Similar to the observations reported in the literature[16, 17] the inflow Ti profile was not found to have a significant impact on the estimated C_P values. As can be seen in Fig. 6(a), the C_P curves obtained in the laminar and homogeneous turbulent inflows can be seen to be overlapping at $TSR < 4$, however, the C_P values estimated

in the non-homogeneous turbulent inflow can be noticed to be comparatively lower. The differences between the tested cases become more noticeable beyond *TSR* ~ 4. C_P measured in the homogeneous turbulent inflow can be briefly observed to be greater than the C_P in the laminar inflow condition. The maximum C_P obtained in the homogeneous turbulent inflow was found to be ~5% higher than the maximum C_P in the laminar flow and was observed at a slightly higher *TSR*. C_P values measured in the non-homogeneous turbulent inflow were lower than the laminar inflow case for the most part; the maximum C_P, however, was comparable (~1.5% lower) and was observed at a higher *TSR* as in the case of the homogeneous turbulent inflow. The effect of the inflow profile was more evident on the measured C_T (see Fig. 6(b)). At *TSR* > 3 (operating range of the turbine) C_T in the homogeneous turbulent inflow was found to be <~7% lower than the corresponding values in the laminar inflow. However, the drop in C_T observed in the non-homogeneous turbulent inflow (in the turbine operating range) was significantly larger in the 15-25%% range and was found to decrease with increasing *TSR*.

2) Standard deviation

The standard deviations of C_P and C_T measurements, $\sigma(C_P)$ and $\sigma(C_T)$ are plotted in Fig. 7. Relative to C_P, $\sigma(C_P)$ is noticeably more sensitive to variations in the inflow at *TSR* > 2.5. $\sigma(C_P)$ in the homogenous turbulent inflow was observed to increase significantly with *TSR*, reaching values 4.5 times the corresponding value in laminar flow at the maximum *TSR* tested. $\sigma(C_P)$ measured in the non-homogenous turbulent inflow was also observed to be greater than its counterparts in the laminar inflow, however by a considerably smaller margin; < 30% within 3<*TSR*<5.7. A similar trend was noticeable in $\sigma(C_T)$ as well. $\sigma(C_T)$ in the homogenous turbulent inflow increased with *TSR*, reaching values 2.7 times the corresponding value in the laminar flow at *TSR* =5.7. Increase in $\sigma(C_T)$ for the non-homogenous turbulent flow was more modest; the maximum increase in $\sigma(C_T)$ measured in the non-homogenous turbulent flow was found to be ~30% of the corresponding value in the laminar flow at *TSR*=5.7.

The obtained experimental measurements indicate that thrust and torque fluctuations experienced by the rotor, scale with the averaged turbulence intensity across the rotor. The homogeneous turbulent inflow, as stated earlier, has a larger depth-averaged Ti than the non-homogeneous and laminar flow cases, and therefore leads to significantly larger thrust and torque fluctuations. Such load fluctuations can have a significant impact on the design requirements for the different turbine components and their operational life. Therefore, they must be estimated and accounted for in the design phase itself to produce robust and efficient turbine systems[17].

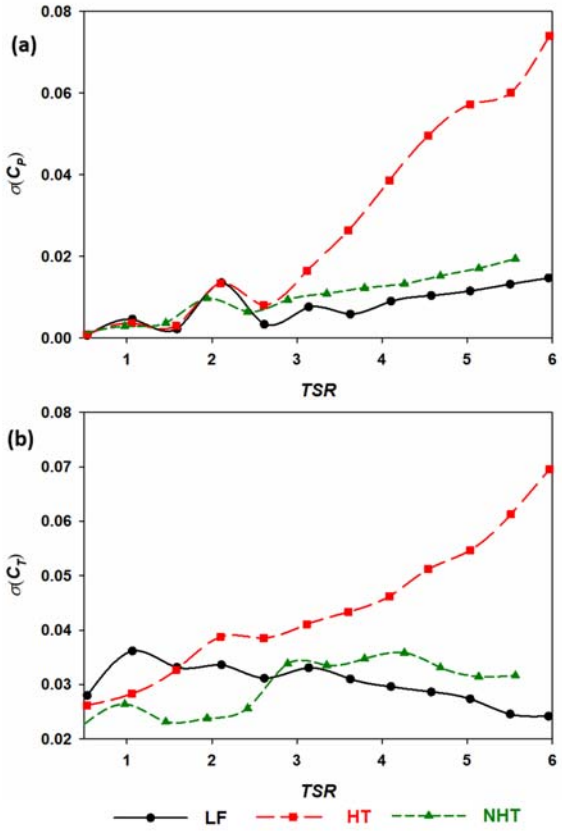

Fig. 7. Effect of inflow conditions on (a) $\sigma(C_P)$, (b) $\sigma(C_T)$

F. Rotor wake characteristics

1) Wake velocity deficit

The wake velocity deficit, *U** is a non-dimensional parameter that characterizes the drop in streamwise velocities due to energy extraction by the rotor. It is defined as

$$U^*(Y,Z) = \frac{U\ (Y,Z) - U_{WAKE}(Y,Z)}{U\ (Y,Z)} \qquad (10)$$

where, $U_{WAKE}(Y,Z)$ is the time-averaged velocity at a specific location, and $U(Y,Z)$ is the corresponding time-averaged inflow velocity value. *U** profiles downstream of the rotor at *X*/*D* = 0.5, 2 are plotted in Fig. 8. A low-speed wake region with a width close to the diameter of the rotor and a region of flow acceleration around the rotor (due to blockage effects) can be identified in all three cases. At *X*/*D* = 0.5, all three cases have a top-hat like *U** profile representative of an undisturbed near wake region. A region of faster moving flow (lower *U**) can be noticed within -0.25 < *Z*/*D* < 0.25, (most prominent in the laminar inflow); this region is hypothesized to be an artifact of the lower solidity of the rotor close to the hub (see Fig. 1). The local shrinkage in frontal rotor area is expected to provide a lesser blockage and an easier passage for the incoming flow, resulting in a noticeable increase of local streamwise velocities. The maximum velocity deficit observed (~0.46-0.48) at *X*/*D* = 0.5 were found to be comparable in the three inflow cases. While the *U** profiles corresponding to the

laminar and homogeneous turbulent inflows were appreciably symmetric about the turbine axis, the U^* profile corresponding to the non-homogeneous inflow was identifiably asymmetric. The U^* values in the upper half of the rotor wake were found to be noticeably lower; the maximum velocity deficit in the upper half, which experienced a faster and less turbulent inflow was estimated to be ~10% lower than the corresponding values in the lower half, which experienced a slower and more turbulent inflow. This observation is expected to be a consequence of the faster inflow at the upper half of the rotor and the reduced solidity of rotor close to the hub; the faster flow finds its way into the wake of the rotor through the region close to the rotor hub. This is reflected in the more noticeable drop in U^* close to the rotor hub at Z/D = 0.2. Unsurprisingly, the bypass velocity below the rotor (at Z/D = -0.6) was 35% faster than its counterpart in the upper half.

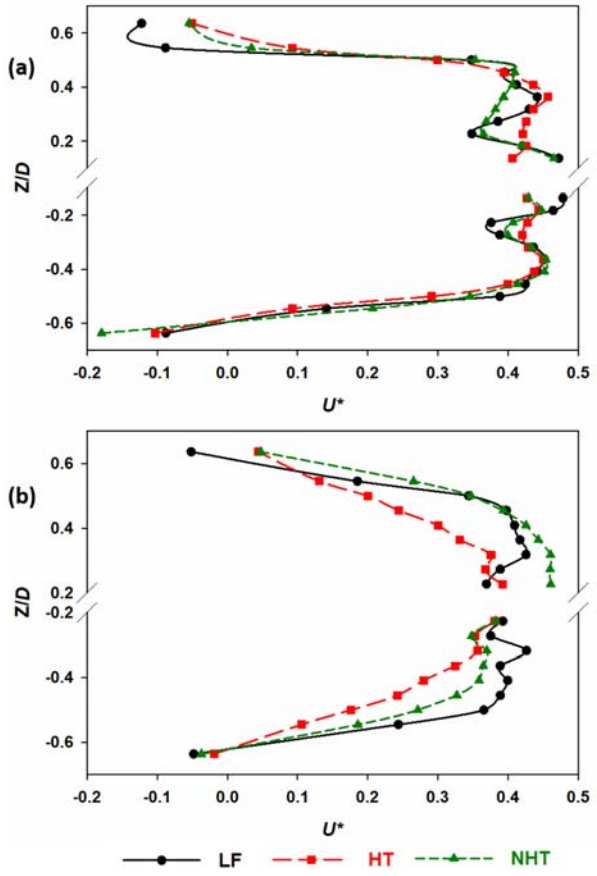

Fig. 8. Depth-wise variation of velocity deficit U^*, at (a) X/D = 0.5, (b) X/D = 2

The effect of inflow characteristics becomes more conspicuous with the downstream evolution of the wake. At X/D = 2, the bypass flow acceleration was found to decrease in all three inflow cases. The tendency of wake re-energization was suggested by the drop in maximum velocity deficits at X/D = 2; maximum U^* corresponding to the laminar inflow dropped by ~10% whereas the same in the homogeneous turbulent inflow dropped by 15% hinting towards the enhanced cross stream momentum transfer in higher ambient turbulence. The asymmetric characteristic of the wake in the non-homogeneous inflow was more pronounced at X/D = 2. Unlike the trend observed at X/D = 0.5, the U^* values in the upper half of the rotor wake had evolved to larger values in comparison to their counterparts in the lower half. In other words, U^* values in the lower half of the rotor wake dropped considerably, while the corresponding values in the upper half remained largely unaltered. This trend can be correlated with the effect of ambient turbulence. The lower wake, being in a more turbulent environment, is likely to undergo a quicker re-energization in comparison to the upper wake which is in a less turbulent environment. The maximum velocity deficit in the lower half was found to be ~20% lesser that the corresponding values in the upper half. Being sufficiently downstream of the rotor, the local flow acceleration close to the hub had no effect of U^* profiles at X/D= 2.

2) Streamwise turbulence intensity

Profiles of streamwise turbulence intensity, Ti, in the wake of the rotor are plotted in Fig. 9. At X/D = 0.5, a gradual rise of Ti in regions close to the hub, and Ti peaks close to the rotor tips are observable in all the three inflow conditions. In the homogeneous turbulent inflow, Ti across the wake was symmetric about the turbine axis and larger than the corresponding values in the laminar and non-homogeneous turbulent inflows; Ti measured at the peaks near the rotor tip were found to be as high as ~ 21%, and in the annular intermediate region between the rotor tip and hub was found to be in the 11-15% range. An asymmetric character was evident in the wake Ti profile corresponding to the non-homogeneous turbulent inflow. Ti close to the bottom tip of the rotor (in the more turbulent inflow) was found to be ~28% larger than the corresponding value in the upper half of the wake; Ti in the lower intermediate region (9-10%) can also be noticed to be larger than its counterparts in the upper intermediate region (5-7%). The depth-wise variation of Ti in the laminar inflow was observed to be symmetric for the most part, except at the Ti peaks close to the rotor tips; the upper tip closer to the free surface was considerably more turbulent, reaching values of Ti close to 15%, whereas, the lower peak close to the tunnel floor was contained slightly below a value of Ti=9%. The magnitudes of Ti in the wake for the homogeneous and non-homogeneous turbulent inflows were observed to drop with the downstream propagation of the wake (see Fig. 9(b)). At X/D = 2, Ti values corresponding to the homogeneous turbulent inflow drop to values in the 10-15% range, and the same in the non-homogeneous turbulent inflow drops to an even lower, 5-15% range. The asymmetric character of the non-homogeneous turbulent inflow is still evident at X/D = 2; the Ti peak close to the lower tip of the rotor was ~22% higher than the peak at the upper tip of the rotor. The turbulence in the lower intermediate region was also

noticeably higher. The *Ti* profile in the laminar flow was noticeably less diffused. Local spikes in *Ti* ranging in values between 11-13% were discernible at *X*/*D* = 2. However, the asymmetry in the magnitudes of peaks close to the rotor tip was found to be reduced; the peaks were comparable with *Ti* values in the 11-13% range.

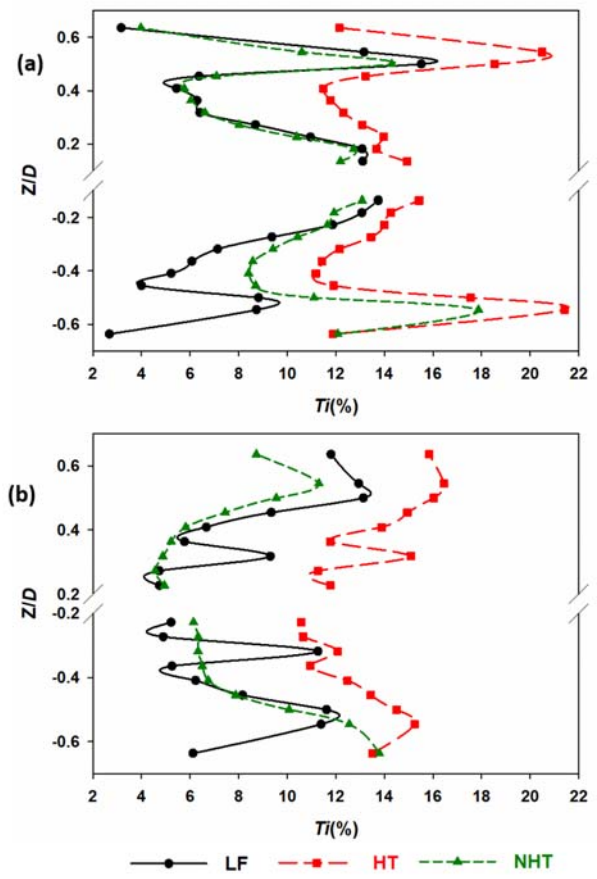

Fig. 9. Depth-wise variation of streamwise turbulence intensity *Ti*, at (a) *X*/*D* = 0.5, (b) *X*/*D* = 2

3) *Reynolds Stresses*

Fig. 10 plots the Reynolds stress component R_{XZ} at the downstream location *X*/*D*=0.5, 2. Similar to the trends observed in wake *Ti*, R_{XZ} peaks can be noticed in wake regions close to the rotor tip, further emphasizing the role of the shear layer in the production of turbulence in the rotor wake. The symmetric nature of the homogeneous turbulent inflow and the asymmetric nature of non-homogeneous inflow is reflected in the depth-wise R_{XZ} profiles as well, specifically in terms of the maximum R_{XZ} values observed in the peaks close to the rotor tips. In the homogeneous turbulent inflow, the peaks were comparable with a magnitude of R_{XZ} =~0.10; in the non-homogeneous case, on the other hand, the peak in the lower wake was larger than its upper wake counterpart by ~33%. Considerable depth-wise variation/fluctuation of R_{XZ} in the intermediate regions was noticeable in all the inflow conditions tested. R_{XZ} magnitudes corresponding to the laminar flow were lower than the turbulent inflow cases for the most part. Further downstream at *X*/*D* = 2, the R_{XZ} profiles corresponding to the turbulent inflow cases become more diffused with noticeably lesser fluctuations in the intermediate regions. Large values comparable to the magnitudes at *X*/*D* = 0.5 persist in the regions close to the rotor tip, however, can be noticed to be less concentrated at the rotor tips, suggesting a higher level of wake mixing. The asymmetric nature incited by the non-homogeneous turbulent inflow can be noticed at *X*/*D* = 2 as well, via the larger stresses observed in, the lower half of the rotor. Unlike the turbulent inflow cases, the stresses in the laminar inflow were found to increase at *X*/*D* = 2, reaching maximum values comparable to the values observed in the turbulent inflow. This observation agrees with findings reported in the literature, which state that, for low levels of ambient turbulence, the mixing intensifies not immediately downstream of the rotor, but at downstream distances in the range 5–7*D*[17].

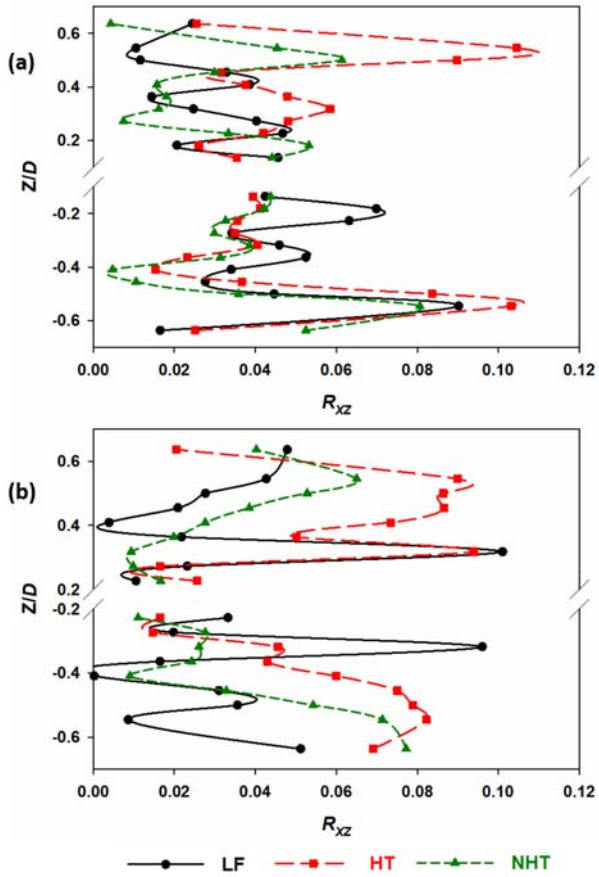

Fig. 10. Depth-wise variation of R_{XZ} Reynolds stresses, at (a) *X*/*D* = 0.5, (b) *X*/*D* = 2

4) *Integral Length Scales*

The evolution of integral length scales *L*, in the wake of the rotor, is illustrated in Fig. 11. It can be seen that the depth-wise profile of *L* in the wake of the rotor is notably affected by the inflow characteristics. At *X*/*D* = 0.5 in the laminar inflow, *L* was found to be appreciably uniform across the wake with values in the 0.0038m – 0.0063m range. Although to a lesser extent, depth-wise uniformity was also observable in the more turbulent non-

homogeneous inflow with L varying in the 0.0076m-0.0203m range. The homogenous turbulent inflow case, on the other hand, resulted in a noticeably larger and non-uniform depth-wise variation of L (0.0102m-0.0635m) at X/D = 0.5. L estimated in the regions close to the rotor hub and tip were smaller than the values calculated in the intermediate regions. This tendency, though significantly less pronounced, can be noticed in the laminar and non-homogeneous turbulent inflow cases as well.

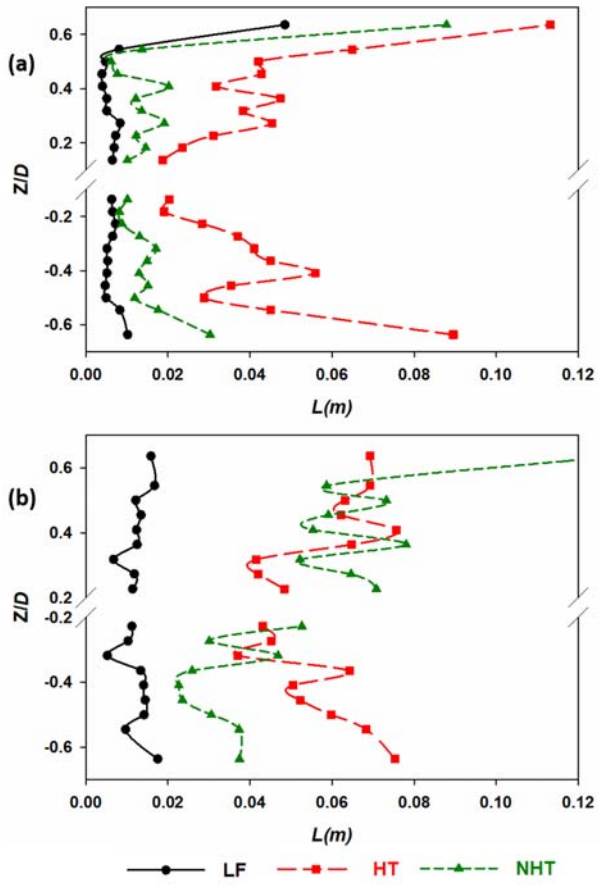

Fig. 11. Depth-wise variation of integral length scales L, at (a) X/D = 0.5, (b) X/D = 2

With downstream propagation, the integral length scales were found to grow in all three tested cases (see Fig. 11 (b)). At X/D = 2, L across the wake in the laminar inflow remained uniform in the 0.0051m-0.0127m range, and the depth-wise variability of L in the homogeneous turbulent inflow was found to remain contained within the comparatively smaller 0.0381m-0.0762m range. Unlike the symmetric profile observed at X/D = 0.5, an asymmetric L profile is noticeable at X/D = 2 in the non-homogeneous turbulent inflow. In this case, L showed the tendency to increase with distance from the bottom of the tunnel (grow with the rise in mean flow velocity). In the slower, more turbulent lower half of the wake, L varied from a value of 0.0254m at Z/D =0.4 to 0.0508m at Z/D = 0.2, and in the faster, less turbulent upper half of the wake, L varied from a value of 0.0508m at Z/D=0. to 0.0762m at Z/D = 0.5.

IV. Conclusion

The experimental results presented in this paper illustrates the effect of a non-homogeneous turbulent inflow on the performance and near wake characteristics of a 1:20 laboratory-scale tidal turbine model. The main findings of the study can be summarised as follows:

- Inflow turbulence and non-homogeneity were not found to have a significant impact on the power curve of the tested tidal turbine. The maximum C_P measured in the non-homogeneous turbulent inflow was ~1.6% lower than the maximum C_P obtained in the laminar inflow and was observed at a comparatively higher TSR.
- The effect on the time-averaged thrust coefficients was noteworthy. C_T values measured (in the turbine operating range) in the non-homogeneous turbulent inflow were ~15-20% lower than their counterparts in the laminar inflow.
- The effects of inflow turbulence levels were better reflected in the measured torque and thrust fluctuations. The standard deviation of the experienced turbine loads was found to scale with the depth-averaged value of Ti. The maximum increase in $\sigma(C_P)$ and $\sigma(C_T)$ measured in the non-homogeneous turbulent inflow was found to be 30% (when compared to the laminar inflow case). The corresponding increase in the homogeneous turbulent inflow was significantly larger (4.5 times and 2.7 times respectively).
- An asymmetric character was evident in the downstream evolution of the velocity deficit profile in the non-homogeneous turbulent inflow case. By X/D = 2, the portion of the wake in the more turbulent inflow region (lower half) showed the tendency to recover streamwise velocities faster than the portion of the wake in the less turbulent region (upper half).
- The effect of inflow non-homogeneity on the measured wake turbulence intensities was found to be more immediate. Ti in the lower portion of the wake (from rotor hub to tip) was consistently more than the Ti values in the upper portion of the wake starting from X/D=0.5 itself. A similar trend was reflected in the measured Reynolds stresses as well.
- As observed in the case of wake velocity deficit, the response of integral length scales in the rotor wake to the inflow inhomogeneity was noticed to be more gradual. An asymmetric depth-wise variation of L becomes noticeably only at X/D = 2, with L showing the tendency to grow faster with distance from the bottom boundary.

References

1. IPCC, *Global Warming of 1.5° C*. 2018, United Nations.
2. Watchorn, M. and T. Trapp. *Tidal stream renewable offshore power generation (TS-Ropg)*. in *World renewable energy congress VI*. 2000: Elsevier.

3. Howland, M.F., et al., *Wake structure in actuator disk models of wind turbines in yaw under uniform inflow conditions.* Journal of renewable and sustainable energy, 2016. **8**(4): p. 043301.
4. Morandi, B., et al., *Experimental investigation of the near wake of a horizontal axis tidal current turbine.* International Journal of Marine Energy, 2016. **14**: p. 229-247.
5. Bahaj, A., et al., *Power and thrust measurements of marine current turbines under various hydrodynamic flow conditions in a cavitation tunnel and a towing tank.* Renewable Energy, 2007. **32**(3): p. 407-426.
6. Kolekar, N. and A. Banerjee, *A coupled hydro-structural design optimization for hydrokinetic turbines.* Journal of renewable and sustainable energy, 2013. **5**(5): p. 053146.
7. Milne, I., et al., *Blade loads on tidal turbines in planar oscillatory flow.* Ocean Engineering, 2013. **60**: p. 163-174.
8. Myers, L. and A. Bahaj. *Near wake properties of horizontal axis marine current turbines*. in *Proceedings of the 8th European wave and tidal energy conference*. 2009: Uppsala, Sweden.
9. Chen, Y., et al., *Experimental study of wake structure behind a horizontal axis tidal stream turbine.* Applied Energy, 2017. **196**: p. 82-96.
10. Kolekar, N. and A. Banerjee, *Performance characterization and placement of a marine hydrokinetic turbine in a tidal channel under boundary proximity and blockage effects.* Applied Energy, 2015. **148**: p. 121-133.
11. Myers, L. and A. Bahaj, *Experimental analysis of the flow field around horizontal axis tidal turbines by use of scale mesh disk rotor simulators.* Ocean Engineering, 2010. **37**(2): p. 218-227.
12. Sun, X., J. Chick, and I. Bryden, *Laboratory-scale simulation of energy extraction from tidal currents.* Renewable Energy, 2008. **33**(6): p. 1267-1274.
13. Stallard, T., et al., *Interactions between tidal turbine wakes: experimental study of a group of three-bladed rotors.* Phil. Trans. R. Soc. A, 2013. **371**(1985): p. 20120159.
14. Stallard, T., T. Feng, and P. Stansby, *Experimental study of the mean wake of a tidal stream rotor in a shallow turbulent flow.* Journal of Fluids and Structures, 2015. **54**: p. 235-246.
15. Tedds, S., I. Owen, and R. Poole, *Near-wake characteristics of a model horizontal axis tidal stream turbine.* Renewable Energy, 2014. **63**: p. 222-235.
16. Blackmore, T., L.E. Myers, and A.S. Bahaj, *Effects of turbulence on tidal turbines: Implications to performance, blade loads, and condition monitoring.* International Journal of Marine Energy, 2016. **14**: p. 1-26.
17. Mycek, P., et al., *Experimental study of the turbulence intensity effects on marine current turbines behaviour. Part I: One single turbine.* Renewable Energy, 2014. **66**: p. 729-746.
18. Zhou, Z., et al., *Developments in large marine current turbine technologies–A review.* Renewable and Sustainable Energy Reviews, 2017. **71**: p. 852-858.
19. Blackmore, T., et al., *Influence of turbulence on the drag of solid discs and turbine simulators in a water current.* Experiments in Fluids, 2014. **55**(1): p. 1637.
20. Blackmore, T., W. Batten, and A. Bahaj. *Influence of turbulence on the wake of a marine current turbine simulator*. in *Proc. R. Soc. A*. 2014: The Royal Society.
21. Mycek, P., et al., *Experimental study of the turbulence intensity effects on marine current turbines behaviour. Part II: Two interacting turbines.* Renewable Energy, 2014. **68**: p. 876-892.
22. O'Rourke, F., et al., *Hydrodynamic performance prediction of a tidal current turbine operating in non-uniform inflow conditions.* Energy, 2015. **93**: p. 2483-2496.
23. Ahmed, U., et al., *Fluctuating loads on a tidal turbine due to velocity shear and turbulence: comparison of CFD with field data.* Renewable Energy, 2017. **112**: p. 235-246.
24. Makita, H., *Realization of a large-scale turbulence field in a small wind tunnel.* Fluid Dynamics Research, 1991. **8**: p. 53-64.
25. Lam, W.-H., L. Chen, and R. Hashim, *Analytical wake model of tidal current turbine.* Energy, 2015. **79**: p. 512-521.
26. Vinod, A., A. Lawrence, and A. Banerjee. *Effects of Free Stream Turbulence on Tidal Turbines. Part II - Turbine Performance and Near Wake Characteristics*. in *12th European Wave and Tidal Energy Conference*. 2017. Cork, Ireland.
27. Poorte, R.E.G. and A. Biesheuvel, *Experiments on the motion of gas bubbles in turbulence generated by an active grid.* Journal of Fluid Mechanics, 2002. **461**: p. 127-154.
28. Goring, D.G. and V.I. Nikora, *Despiking acoustic Doppler velocimeter data.* Journal of Hydraulic Engineering, 2002. **128**(1): p. 117-126.